Advances in bifurcations and dynamics of low-dimensional maps.

Indranil Ghosh
https://indrag49.github.io

School of Mathematical and Computational Sciences
Massey University, Palmerston North, New Zealand

March 10, 2025

Border-collision normal form

- Piecewise-linear maps arise when modeling systems with switches, thresholds and other abrupt events.
- In our project, we study the two-dimensional *border-collision normal form* (Nusse & Yorke, 1992), given by

$$f_\xi(x,y) = \begin{cases} \begin{bmatrix} \tau_L & 1 \\ -\delta_L & 0 \end{bmatrix} \begin{bmatrix} x \\ y \end{bmatrix} + \begin{bmatrix} 1 \\ 0 \end{bmatrix}, & x \le 0, \\ \begin{bmatrix} \tau_R & 1 \\ -\delta_R & 0 \end{bmatrix} \begin{bmatrix} x \\ y \end{bmatrix} + \begin{bmatrix} 1 \\ 0 \end{bmatrix}, & x \ge 0. \end{cases}$$

- Here $(x,y) \in \mathbb{R}^2$, and $\xi = (\tau_L, \delta_L, \tau_R, \delta_R) \in \mathbb{R}^4$ are the parameters.

Phase portrait of a chaotic attractor

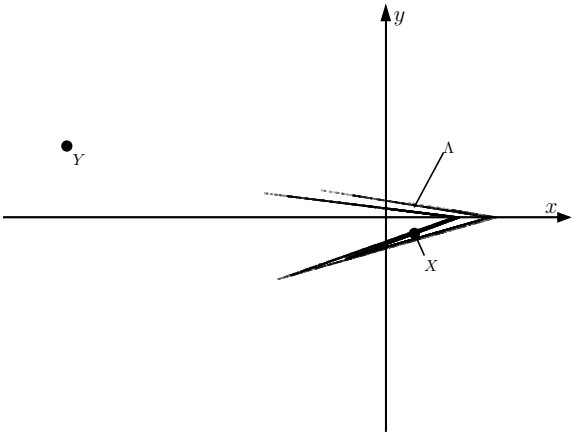

Figure: A sketch of the phase portrait of f_ξ with $\xi \in \Phi_{\mathrm{BYG}}$.

Renormalisation operator

- Renormalisation involves showing that, for some members of a family of maps, a higher iterate or induced map is conjugate to different member of this family of maps.
- Although the second iterate f_ξ^2 has four pieces, relevant dynamics arise in only two of these. We have

$$f_\xi^2(x,y) = \begin{cases} \begin{bmatrix} \tau_L\tau_R - \delta_L & \tau_R \\ -\delta_R\tau_L & -\delta_R \end{bmatrix} \begin{bmatrix} x \\ y \end{bmatrix} + \begin{bmatrix} \tau_R + 1 \\ -\delta_R \end{bmatrix}, & x \le 0, \\ \begin{bmatrix} \tau_R^2 - \delta_R & \tau_R \\ -\delta_R\tau_R & -\delta_R \end{bmatrix} \begin{bmatrix} x \\ y \end{bmatrix} + \begin{bmatrix} \tau_R + 1 \\ -\delta_R \end{bmatrix}, & x \ge 0. \end{cases}$$

Renormalisation operator

- Now f_ξ^2 can be transformed to $f_{g(\xi)}$, where g is the *renormalisation operator* (Ghosh & Simpson, 2022.) $g : \mathbb{R}^4 \to \mathbb{R}^4$, given by

$$\begin{aligned}
\tilde{\tau}_L &= \tau_R^2 - 2\delta_R, \\
\tilde{\delta}_L &= \delta_R^2, \\
\tilde{\tau}_R &= \tau_L \tau_R - \delta_L - \delta_R, \\
\tilde{\delta}_R &= \delta_L \delta_R.
\end{aligned}$$

- We perform a coordinate change to put f_ξ^2 in the normal form :

$$\begin{bmatrix} \tilde{x}' \\ \tilde{y}' \end{bmatrix} = \begin{cases} \begin{bmatrix} \tilde{\tau}_L & 1 \\ -\tilde{\delta}_L & 0 \end{bmatrix} \begin{bmatrix} \tilde{x} \\ \tilde{y} \end{bmatrix} + \begin{bmatrix} 1 \\ 0 \end{bmatrix}, & \tilde{x} \leq 0, \\ \begin{bmatrix} \tilde{\tau}_R & 1 \\ -\tilde{\delta}_R & 0 \end{bmatrix} \begin{bmatrix} \tilde{x} \\ \tilde{y} \end{bmatrix} + \begin{bmatrix} 1 \\ 0 \end{bmatrix}, & \tilde{x} \geq 0. \end{cases}$$

Results

- We consider the parameter region

$$\Phi = \left\{ \xi \in \mathbb{R}^4 \middle| \tau_L > \delta_L + 1, \delta_L > 0, \tau_R < -(\delta_R + 1), \delta_R > 0 \right\}.$$

- Let

$$\phi^+(\xi) = \zeta_0 = \delta_R - (\tau_R + \delta_L + \delta_R - (1 + \tau_R)\lambda_L^u)\lambda_L^u.$$

- The stable and the unstable manifolds of the fixed point Y intersect if and only if $\phi^+(\xi) \leq 0$.
- The attractor is often destroyed at $\phi^+(\xi) = 0$ which is a homoclinic bifurcation (Banerjee, Yorke & Grebogi, 1998), and thus focused their attention on the region

$$\Phi_{\mathrm{BYG}} = \left\{ \xi \in \Phi \middle| \phi^+(\xi) > 0 \right\}.$$

Results

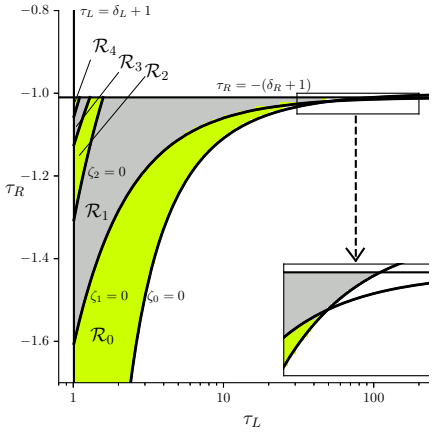

Figure: The sketch of two-dimensional cross-section of Φ_{BYG} when $\delta_L = \delta_R = 0.01$.

Theorem (Ghosh & Simpson, 2022)

The $\mathcal{R}_n$ are non-empty, mutually disjoint, and converge to the fixed point $(1, 0, -1, 0)$ as $n \to \infty$. Moreover,

$$\Phi_{\mathrm{BYG}} \subset \bigcup_{n=0}^{\infty} \mathcal{R}_n.$$

Let,

$$\Lambda(\xi) = \mathrm{cl}(W^u(X)).$$

Theorem (Ghosh & Simpson, 2022)

For the map f_ξ with any $\xi \in \mathcal{R}_0$, $\Lambda(\xi)$ is bounded, connected, and invariant. Moreover, $\Lambda(\xi)$ is chaotic (positive Lyapunov exponent).

Theorem (Ghosh & Simpson, 2022)

For any $\xi \in \mathcal{R}_n$ where $n \geq 0$, $g^n(\xi) \in \mathcal{R}_0$ and there exist mutually disjoint sets $S_0, S_1, \ldots, S_{2^n-1} \subset \mathbb{R}^2$ such that $f_\xi(S_i) = S_{(i+1) \bmod 2^n}$ and

$$f_\xi^{2^n}|_{S_i} \text{ is affinely conjugate to } f_{g^n(\xi)}|_{\Lambda(g^n(\xi))}$$

for each $i \in \{0, 1, \ldots, 2^n - 1\}$. Moreover,

$$\bigcup_{i=0}^{2^n-1} S_i = \mathrm{cl}(W^u(\gamma_n)),$$

where γ_n is a saddle-type periodic solution of our map f_ξ having the symbolic itinerary $\mathcal{F}^n(R)$ given by Table 1.

Results

n	$\mathcal{F}^n(\mathcal{W})$
0	R
1	LR
2	$RRLR$
3	$LRLRRRLR$
4	$RRLRRRLRLRLRRRLR$

Table: The first 5 words in the sequence generated by repeatedly applying the substitution rule $(L, R) \mapsto (RR, LR)$ to $\mathcal{W} = R$.

Results

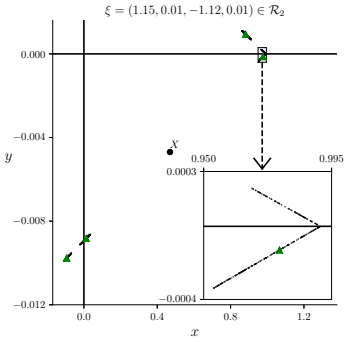
$\xi = (1.15, 0.01, -1.12, 0.01) \in \mathcal{R}_2$
0.000
−0.004
−0.008
−0.012
y
0.0
0.4
0.8
1.2
x
X
0.950
0.995
0.0003
−0.0004

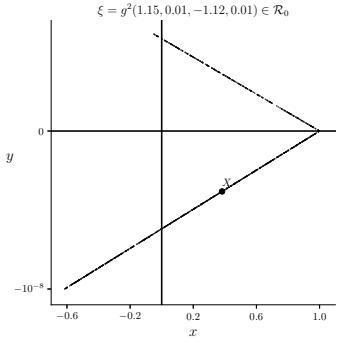
$\xi = g^2(1.15, 0.01, -1.12, 0.01) \in \mathcal{R}_0$
0
-10^{-8}
y
−0.6
−0.2
0.2
0.6
1.0
x
X

Devaney Chaos

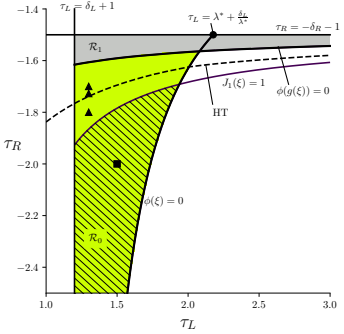

(a) $\delta_L = 0.2$, $\delta_R = 0.5$

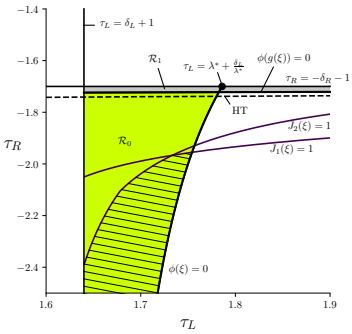

(b) $\delta_L = 0.64$ and $\delta_R = 0.7$

Devaney Chaos

Theorem (Ghosh & Simpson, 2022)

Let $\xi \in \Phi_{\mathrm{BYG}}$ and suppose $J_1(\xi) > 1$ and $\lambda_L^s + |\lambda_R^s| < 1$. Then $W^s(X)$ is dense in a triangular region containing Λ.

Theorem (Ghosh & Simpson, 2022)

Let $\xi \in \Phi_{\mathrm{BYG}}$ and suppose $J_1(\xi) > 1$ and $J_2(\xi) < 1$. Then, f_ξ is chaotic in the sense of Devaney on Λ.

Generalised parameter region

Now we consider the more generalised parameter region considering the orientation-reversing and non-invertible cases,

$$\Phi = \left\{ \xi \in \mathbb{R}^4 \;\middle|\; \tau_L > |\delta_L + 1|, \tau_R < -|\delta_R + 1| \right\}.$$

Typical phase portraits

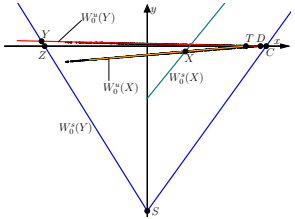

(a) $\delta_L > 0, \delta_R > 0$

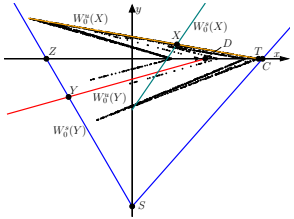

(b) $\delta_L < 0, \delta_R < 0$

Figure: Typical phase portraits of the chaotic attractor for the invertible case ($\delta_L \delta_R > 0$).

Typical phase portraits

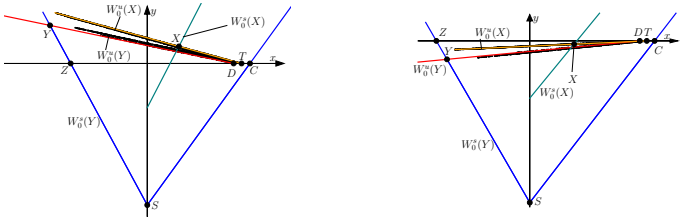

(a) $\delta_L > 0, \delta_R < 0$ (b) $\delta_L < 0, \delta_R > 0$

Figure: Typical phase portraits of the chaotic attractor for the non-invertible case ($\delta_L \delta_R < 0$).

Invariant expanding cones

Chaos in Φ_{BYG} can be proved by constructing an invariant expanding cone in tangent space (Glendinning & Simpson, 2021). We have extended this to Φ.

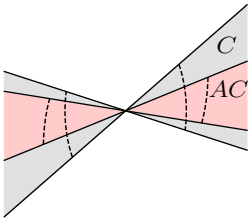

Figure: A sketch of an invariant expanding cone C and its image $AC = \{Av | v \in C\}$, given $A \in \mathbb{R}^{2\times 2}$.

Robust Chaos in a generalised setting

Theorem (Ghosh, McLachlan, & Simpson, 2023)

For any $\xi \in \Phi_{\text{trap}} \cap \Phi_{\text{cone}}$, the normal form f_ξ has a topological attractor with a positive Lyapunov exponent.

Robust Chaos in a generalised setting

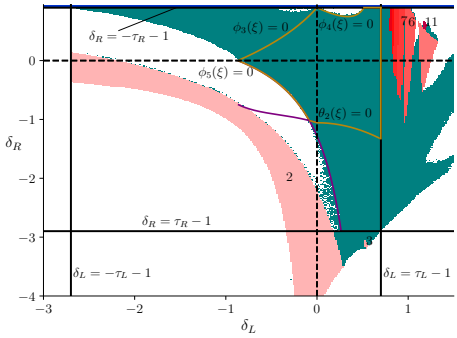

Figure: A 2D slice of $\Phi_{\text{trap}} \cap \Phi_{\text{cone}} \subset \mathbb{R}^4$.

The orientation-reversing case

- Let

$$\Phi^{(2)} = \{\xi \in \Phi \mid \delta_L < 0, \delta_R < 0\},$$

be the subset of Φ for which the BCNF is orientation-reversing.

- The attractor Λ which is again a closure of the unstable manifold of X faces a crisis at $\zeta_0^{(2)} = 0$ where

$$\zeta_0^{(2)} = \phi^-(\xi) = \delta_R - (\delta_R + \tau_R - (1 + \lambda_R^u)\lambda_L^u)\lambda_L^u .$$

The orientation-reversing case

- Now, $\xi \in \Phi^{(2)}$ implies $g(\xi) \in \Phi^{(1)}$, so we again use the preimages of $\phi^+(\xi) = 0$ under g to define the region boundaries: Specifically we let

$$\mathcal{R}_0^{(2)} = \left\{ \xi \in \Phi^{(2)} \,\middle|\, \phi^-(\xi) > 0, \phi^+(g(\xi)) \leq 0, \alpha(\xi) < 0 \right\},$$
$$\mathcal{R}_n^{(2)} = \left\{ \xi \in \Phi^{(2)} \,\middle|\, \phi^+\left(g^n(\xi)\right) > 0, \phi^+\left(g^{n+1}(\xi)\right) \leq 0, \alpha(\xi) < 0 \right\}, \qquad \text{for all } n \geq 1.$$

  where

$$\alpha(\xi) = \tau_L \tau_R + (\delta_L - 1)(\delta_R - 1).$$

- This brings us to the proposition

Proposition (Ghosh, McLachlan, & Simpson, 2024)

If $\xi \in \mathcal{R}_n^{(2)}$ with $n \geq 1$, then $g(\xi) \in \mathcal{R}_{n-1}^{(1)}$.

The orientation-reversing case

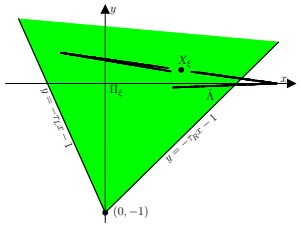

(a) $\xi = \xi_{\text{ex}}^{(2)} \in \mathcal{R}_1^{(2)}$

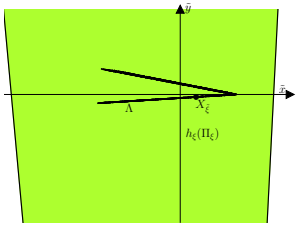

(b) $\xi = g(\xi_{\text{ex}}^{(2)}) \in \mathcal{R}_0^{(1)}$

The non-invertible case $\delta_L > 0, \delta_R < 0$

- Let

$$\Phi^{(3)} = \{\xi \in \Phi \mid \delta_L > 0, \delta_R < 0\},$$

meaning the map is invertible.

- In this region an attractor can be destroyed by crossing the homoclinic bifurcation $\phi^+(\xi) = 0$ or the heteroclinic bifurcation $\phi^-(\xi) = 0$.
- we define

$$\phi_{\min}(\xi) = \min[\phi^+(\xi), \phi^-(\xi)].$$

and

$$\mathcal{R}_n^{(3)} = \left\{\xi \in \Phi^{(3)} \,\middle|\, \phi_{\min}\left(g^n(\xi)\right) > 0,\ \phi_{\min}\left(g^{n+1}(\xi)\right) \leq 0,\ \alpha(\xi) < 0\right\},$$

for all $n \geq 0$.

The non-invertible case $\delta_L > 0, \delta_R < 0$

- This brings us to a new proposition:

Proposition (Ghosh, McLachlan, & Simpson, 2024)

If $\xi \in \mathcal{R}_n^{(3)}$ *with* $n \geq 1$, *then* $g(\xi) \in \mathcal{R}_{n-1}^{(3)}$.

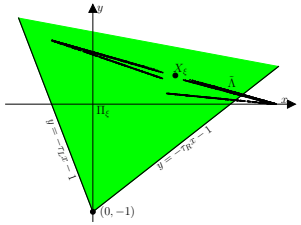

(a) $\xi = \xi_{\text{ex}}^{(3)} \in \mathcal{R}_1^{(3)}$

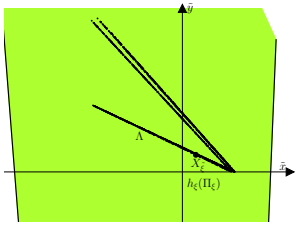

(b) $\xi = g(\xi_{\text{ex}}^{(3)}) \in \mathcal{R}_0^{(3)}$

The non-invertible case $\delta_L < 0, \delta_R > 0$

- It remains for us to consider

$$\Phi^{(4)} = \{\xi \in \Phi \mid \delta_L < 0, \delta_R > 0\},$$

  where the BCNF is again non-invertible.
- In this region the attractor is usually destroyed before the boundaries $\phi^+(\xi) = 0$ and $\phi^-(\xi) = 0$ in a heteroclinic bifurcation that cannot be characterised by an explicit condition on the parameter values.
- Despite the extra complexities in $\Phi^{(4)}$ it still appears that renormalisation is helpful for explaining the bifurcation structure. Let

$$\mathcal{R}_0^{(4)} = \left\{\xi \in \Phi^{(4)} \;\middle|\; \phi_{\min}(\xi) > 0,\ \phi_{\min}(g(\xi)) \leq 0,\ \alpha(\xi) < 0\right\}.$$
$$\mathcal{R}_n^{(4)} = \left\{\xi \in \Phi^{(4)} \;\middle|\; \phi_{\min}(g^n(\xi)) > 0,\ \phi_{\min}(g^{n+1}(\xi)) \leq 0,\ \alpha(\xi) < 0, \alpha(g(\xi)) < 0\right\}. \quad (1)$$

The non-invertible case $\delta_L < 0, \delta_R > 0$

- This brings us to the new propostion:

Proposition (Ghosh, McLachlan, & Simpson, 2024)

If $\xi \in \mathcal{R}_n^{(4)}$ *with* $n \geq 1$, *then* $g(\xi) \in \mathcal{R}_{n-1}^{(3)}$.

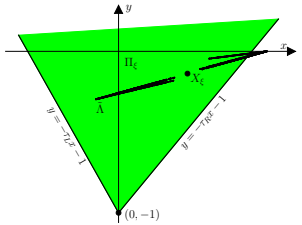

(a) $\xi = \xi_{\text{ex}}^{(4)} \in \mathcal{R}_1^{(4)}$

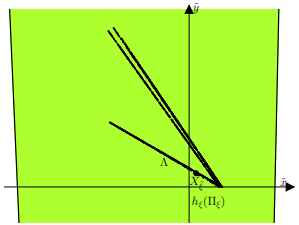

(b) $\xi = g(\xi_{\text{ex}}^{(4)}) \in \mathcal{R}_0^{(3)}$

Numerics

- We verify these bifurcation structures numerically by using Eckstein's greatest common divisor algorithm (Eckstein, 2006), described by Avrutin *et al*, 2007 to estimate from sample orbits the number of connected components in the attractor.

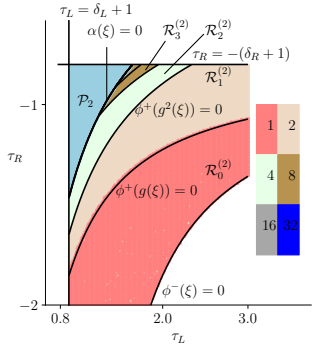

(a) $\delta_L = -0.1, \delta_R = -0.2.$

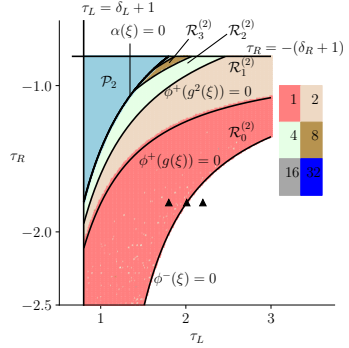

(b) $\delta_L = -0.2, \delta_R = -0.2.$

Numerics

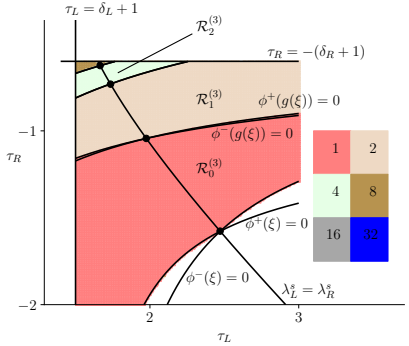

(a) $\delta_L = 0.5, \delta_R = -0.4$.

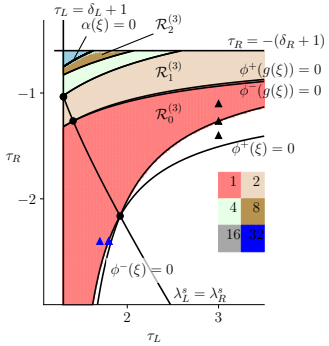

(b) $\delta_L = 0.3, \delta_R = -0.4$.

Numerics

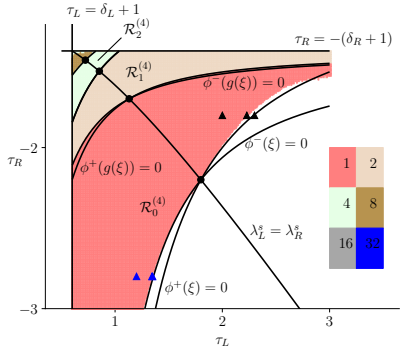

(a) $\delta_L = -0.4, \delta_R = 0.4$.

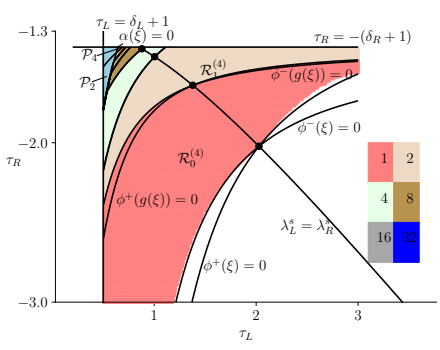

(b) $\delta_L = -0.5, \delta_R = 0.4$.

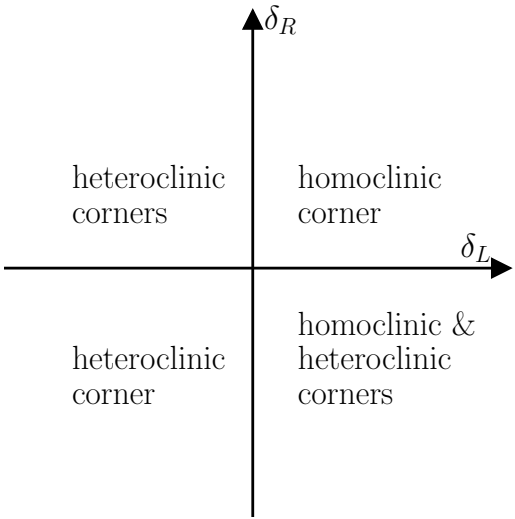
δ_R
heteroclinic corners
homoclinic corner
δ_L
heteroclinic corner
homoclinic & heteroclinic corners

Higher-dimensional setting

- Let $n \geq 2$. Suppose $\alpha > 1$ is an eigenvalue of A_L, and $-\beta < -1$ of A_R with multiplicity one, and all other eigenvalues of A_L and A_R have modulus at most $0 < r < 1$.

Theorem (Ghosh & Simpson, 2024)

Holding the above assumption and

$$r(n-1) < \frac{3}{7}\left(1 - \frac{1}{\alpha}\right), \qquad r(n-1) < \frac{3}{7}\left(1 - \frac{1}{\beta}\right),$$

$$r(n-1) < \frac{1}{10}\left(\frac{1}{\alpha} + \frac{1}{\beta} - 1\right),$$

then f has a topological attractor with a positive Lyapunov exponent.

Higher-dimensional setting

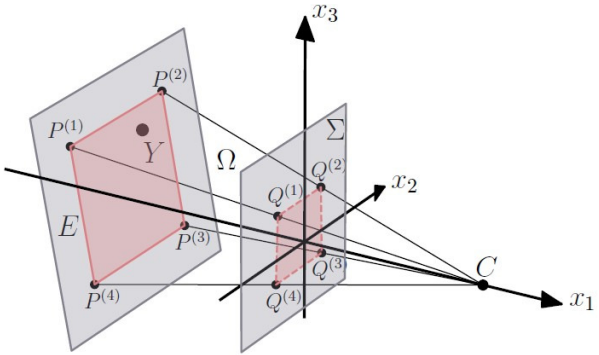

Figure: The construction of a forward invariant region Ω for $n = 3$.

Higher-dimensional setting

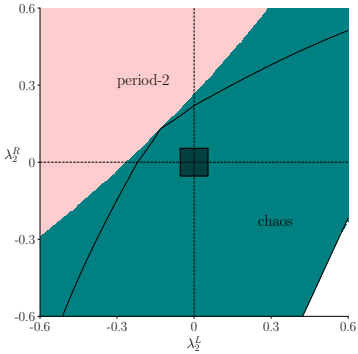

Figure: Robust chaos parameter region for the two-dimensional map, with our higher-dimensional construction portrayed on top of it. We chose $n = 2$ for simplicity.

Future Directions

- We expect our construction in the two-dimensional setting could be adapted to verify robust chaos beyond the boundaries reported.

Future Directions

- We expect our construction in the two-dimensional setting could be adapted to verify robust chaos beyond the boundaries reported.
- It would be interesting to see if renormalisation schemes based on other symbolic substitution rules can be used to explain parameter regimes where the BCNF has attractors with other numbers of components, e.g. three components.

Future Directions

- We expect our construction in the two-dimensional setting could be adapted to verify robust chaos beyond the boundaries reported.
- It would be interesting to see if renormalisation schemes based on other symbolic substitution rules can be used to explain parameter regimes where the BCNF has attractors with other numbers of components, e.g. three components.
- Maps with multiple directions of instability should be just as relevant, giving the possibility of so-called wild chaos, and it remains to treat these scenarios.

Future Directions

- We expect our construction in the two-dimensional setting could be adapted to verify robust chaos beyond the boundaries reported.
- It would be interesting to see if renormalisation schemes based on other symbolic substitution rules can be used to explain parameter regimes where the BCNF has attractors with other numbers of components, e.g. three components.
- Maps with multiple directions of instability should be just as relevant, giving the possibility of so-called wild chaos, and it remains to treat these scenarios.
- Can apply similar sort of renormalisation to the circle map.

Future Directions

- We expect our construction in the two-dimensional setting could be adapted to verify robust chaos beyond the boundaries reported.
- It would be interesting to see if renormalisation schemes based on other symbolic substitution rules can be used to explain parameter regimes where the BCNF has attractors with other numbers of components, e.g. three components.
- Maps with multiple directions of instability should be just as relevant, giving the possibility of so-called wild chaos, and it remains to treat these scenarios.
- Can apply similar sort of renormalisation to the circle map.
- As one application I want to apply n–dimensional construction as the key space for an encryption scheme.

Impact Oscillators

- Many engineering systems involve vibrations and impacts, e.g. impact print hammers, gear assemblies, machinery for milling, bells, and shock absorbers.

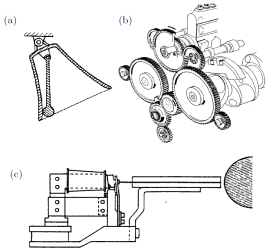

Figure: Examples of simple impacting systems: (a) a bell, (b) a gear assembly, (c) an impact print hammer. Picture taken from *di Bernardo, Champneys, Budd, Kowalczyk, 2008*.

The impact oscillator model

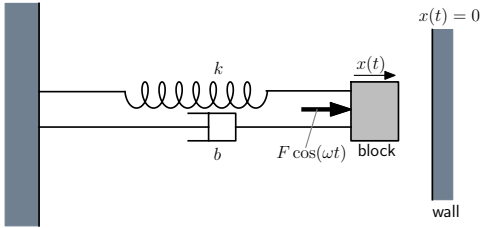

Figure: A hard-impact oscillator model: $\ddot{x} + b\dot{x} + x + 1 = F\cos(\omega t)$ and $\dot{x} \mapsto -r\dot{x}$ whenever $x = 0$.

The impact oscillator model

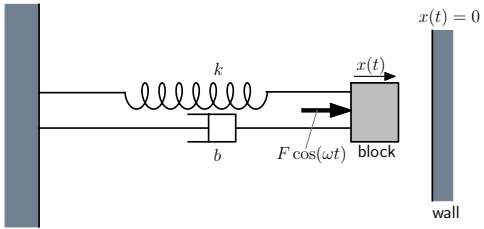

Figure: A hard-impact oscillator model: $\ddot{x} + b\dot{x} + x + 1 = F\cos(\omega t)$ and $\dot{x} \mapsto -r\dot{x}$ whenever $x = 0$.

- If the block hits the wall with zero velocity, this is a *grazing* impact.
- A grazing bifurcation occurs when the limit cycle has a grazing impact.

Literature Survey

- S.W. Shaw, *J. Appl. Mech.*, 1985, S.W. Shaw and P.J. Holmes, *J. Sound Vib.*, 1983: looked into impacting systems, for example mechanical systems having two-sided amplitude contraints
- J. de Weger *et al.*, *Phys. Rev. Lett.*, 1996.: grazing in more applied sense.
- Later works are more experimental: with soft impacts, two symmetrically placed walls, and a block which is a pendulum
- P. T. Piiroinen *et al.*, *J. Nonlinear Sci.*, 2004.
- J. Qiu and Z.C. Feng, *Computers & Structures*, 2000.
- T. Witelski *et al.*, *J. Sound Vib.*, 2014.
- S. Banerjee *et al.*, *Phys. Rev. E*, 2009.
- J. Molenaar *et al.*, *Nonlinearity*, 2001.
- E. Pavlovskaia *et al.*, *Int. J. Bifurcation Chaos*, 2010.

Experimental example

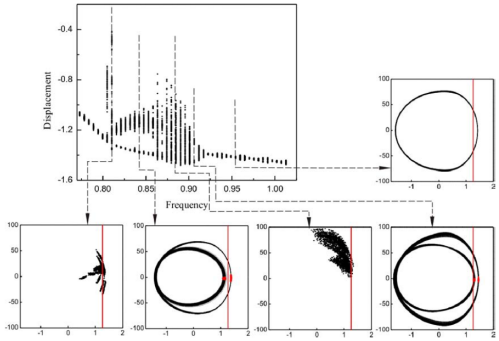

Figure: Bifurcation diagram obtained from the paper by Pavlovskaia *et al.*, Int. J. Bifurcation Chaos, 2010.

Experimental example

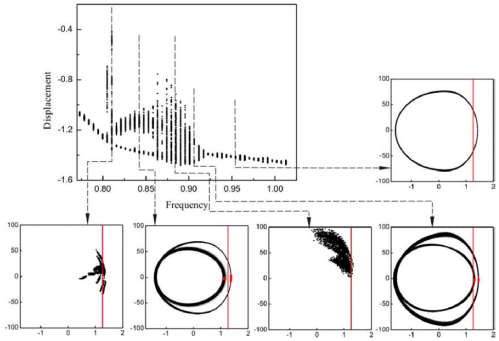

Figure: Bifurcation diagram obtained from the paper by Pavlovskaia *et al.*, Int. J. Bifurcation Chaos, 2010.

- Why does a stable period-two solution appear so close to grazing?

Model

- The nondimensionalised equations of our oscillator model are given by

$$\dot{x} = y,$$
$$\dot{y} = F\cos(\omega t) - by - x - 1,$$

where $x(t)$ and $y(t)$ are the displacement and the velocity of the oscillator with the damping ratio $b > 0$.

Model

- The nondimensionalised equations of our oscillator model are given by

$$\dot{x} = y,$$
$$\dot{y} = F\cos(\omega t) - by - x - 1,$$

  where $x(t)$ and $y(t)$ are the displacement and the velocity of the oscillator with the damping ratio $b > 0$.
- We treat F as the primary bifurcation parameter.

Model

- The nondimensionalised equations of our oscillator model are given by

$$\dot{x} = y,$$
$$\dot{y} = F\cos(\omega t) - by - x - 1,$$

  where $x(t)$ and $y(t)$ are the displacement and the velocity of the oscillator with the damping ratio $b > 0$.
- We treat F as the primary bifurcation parameter.
- The values of F and t that occur at grazing are implicitly given by

$$t_{\text{graz}} = \frac{1}{\omega}\tan^{-1}\left(\frac{b\omega}{1-\omega^2}\right),$$
$$F_{\text{graz}}^2 = (1-\omega^2)^2 + b^2\omega^2.$$

Typical phase portrait

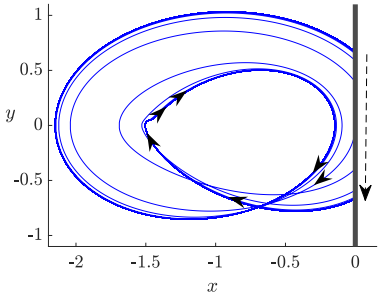

Figure: A typical phase portrait of the impact oscillator.

Bifurcation diagram

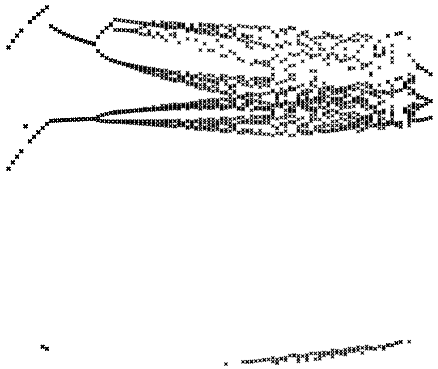

Figure: A typical bifurcation diagram of the impact oscillator.

Poincaré map

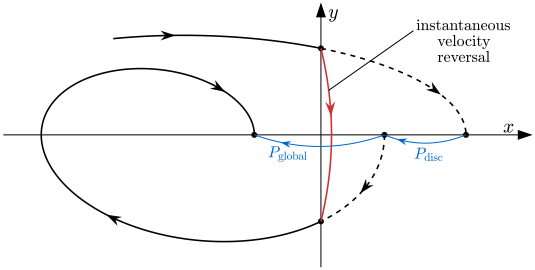

Figure: An illustration of the Poincaré map.

Poincaré map

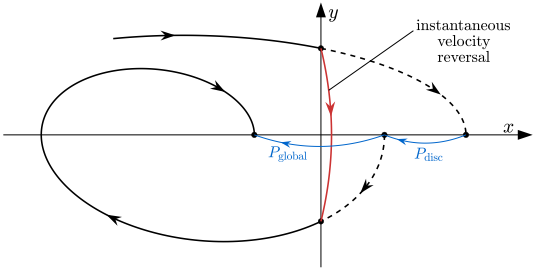

Figure: An illustration of the Poincaré map.

- We use $y = 0$ as the Poincaré section. The map is given by $(x', z') = P(x, z)$ where $z = t - t_{\text{graz}} \mod \frac{2\pi}{\omega}$.
- We evaluate P numerically, using an explicit formula for the flow, and event detection for determining where orbits return to the Poincaré section.

Poincaré map

- The map P can be expressed as

$$P = P_{\text{global}} \circ P_{\text{disc}}.$$

Poincaré map

- The map P can be expressed as

$$P = P_{\text{global}} \circ P_{\text{disc}}.$$

- Here

$$P_{\text{disc}}(x, z; F) = \begin{cases} \begin{bmatrix} x \\ z \end{bmatrix}, & x \leq 0, \\ \begin{bmatrix} r^2 x + \tilde{O}(3) \\ z - \frac{\sqrt{2}}{\omega}(1+r)\sqrt{x} + \tilde{O}(2) \end{bmatrix}, & x > 0. \end{cases}$$

Poincaré map

- To first order, the Taylor expansion of P_{global} about $(x, z; F) = (0, 0; F_{\text{graz}})$ can be written as

$$P_{\text{global}} = K \begin{bmatrix} x \\ z \end{bmatrix} + \frac{F - F_{\text{graz}}}{F_{\text{graz}}} \begin{bmatrix} 1 - a_{11} \\ -a_{21} \end{bmatrix} + O(2),$$

where

$$K = \begin{bmatrix} a_{11} & \omega^2 a_{12} \\ \frac{a_{21}}{\omega^2} & a_{22} \end{bmatrix},$$

and each a_{ij} is the (i, j) entry of

$$A = \exp\left(\frac{2\pi}{\omega} \begin{bmatrix} 0 & 1 \\ -1 & -b \end{bmatrix} \right).$$

- Note that

$$a_{11} = \frac{\lambda_1 e^{\frac{2\pi}{\omega}\lambda_2} - \lambda_2 e^{\frac{2\pi}{\omega}\lambda_2}}{\lambda_1 - \lambda_2}, \qquad a_{12} = \frac{e^{\frac{2\pi}{\omega}\lambda_1} - e^{\frac{2\pi}{\omega}\lambda_2}}{\lambda_1 - \lambda_2},$$

$$a_{21} = -a_{12}, \qquad a_{22} = \frac{(\lambda_1 + b)e^{\frac{2\pi}{\omega}\lambda_2} - (\lambda_2 + b)e^{\frac{2\pi}{\omega}\lambda_1}}{\lambda_1 - \lambda_2},$$

where K has eigenvalues $\lambda_{1,2} = \alpha \pm i\beta$.

- Note that

$$a_{11} = \frac{\lambda_1 e^{\frac{2\pi}{\omega}\lambda_2} - \lambda_2 e^{\frac{2\pi}{\omega}\lambda_2}}{\lambda_1 - \lambda_2}, \qquad a_{12} = \frac{e^{\frac{2\pi}{\omega}\lambda_1} - e^{\frac{2\pi}{\omega}\lambda_2}}{\lambda_1 - \lambda_2},$$

$$a_{21} = -a_{12}, \qquad a_{22} = \frac{(\lambda_1 + b)e^{\frac{2\pi}{\omega}\lambda_2} - (\lambda_2 + b)e^{\frac{2\pi}{\omega}\lambda_1}}{\lambda_1 - \lambda_2},$$

  where K has eigenvalues $\lambda_{1,2} = \alpha \pm i\beta$.

- Here,

$$\alpha = -\frac{b}{2}, \qquad \beta = \sqrt{1 - \frac{b^2}{4}}.$$

- Note that

$$a_{11} = \frac{\lambda_1 e^{\frac{2\pi}{\omega}\lambda_2} - \lambda_2 e^{\frac{2\pi}{\omega}\lambda_2}}{\lambda_1 - \lambda_2}, \qquad a_{12} = \frac{e^{\frac{2\pi}{\omega}\lambda_1} - e^{\frac{2\pi}{\omega}\lambda_2}}{\lambda_1 - \lambda_2},$$

$$a_{21} = -a_{12}, \qquad a_{22} = \frac{(\lambda_1 + b)e^{\frac{2\pi}{\omega}\lambda_2} - (\lambda_2 + b)e^{\frac{2\pi}{\omega}\lambda_1}}{\lambda_1 - \lambda_2},$$

  where K has eigenvalues $\lambda_{1,2} = \alpha \pm i\beta$.

- Here,

$$\alpha = -\frac{b}{2}, \qquad \beta = \sqrt{1 - \frac{b^2}{4}}.$$

- Also K has trace $\tau = 2e^{\frac{2\pi\alpha}{\omega}} \cos\left(\frac{2\pi\beta}{\omega}\right)$ and determinant $\delta = e^{\frac{4\pi\alpha}{\omega}}$.

Numerics

- For a period-p solution of our map P with one point in $x > 0$, this point is a fixed point of $P^p_{\text{global}} \circ P_{\text{disc},R}$.

Numerics

- For a period-p solution of our map P with one point in $x > 0$, this point is a fixed point of $P^p_{\text{global}} \circ P_{\text{disc},R}$.
- *Maximal* periodic solutions are those with exactly one point in $x > 0$ (such periodic solutions are the most likely to be stable because the square-root singularity is highly destabilising)

Numerics

- For a period-p solution of our map P with one point in $x > 0$, this point is a fixed point of $P^p_{\text{global}} \circ P_{\text{disc},R}$.
- *Maximal* periodic solutions are those with exactly one point in $x > 0$ (such periodic solutions are the most likely to be stable because the square-root singularity is highly destabilising)
- Since $P^p_{\text{global}} \circ P_{\text{disc},R}$ is smooth, standard numerical methods like Newton's method can be used to follow fixed points while $x > 0$.

Numerics

- For a period-p solution of our map P with one point in $x > 0$, this point is a fixed point of $P^p_{\text{global}} \circ P_{\text{disc},R}$.
- *Maximal* periodic solutions are those with exactly one point in $x > 0$ (such periodic solutions are the most likely to be stable because the square-root singularity is highly destabilising)
- Since $P^p_{\text{global}} \circ P_{\text{disc},R}$ is smooth, standard numerical methods like Newton's method can be used to follow fixed points while $x > 0$.
- That is, given a guess for (x_0, z_0), we compute (y_1, z_1), (y_2, z_2), and (x_3, z_3), and $(x_4, z_4) = P^p_{\text{global}}(x_3, z_3; F)$. Then let $G(x_0, z_0; F) = (x_4, z_4) - (x_0, z_0)$ and continue zeros of G.

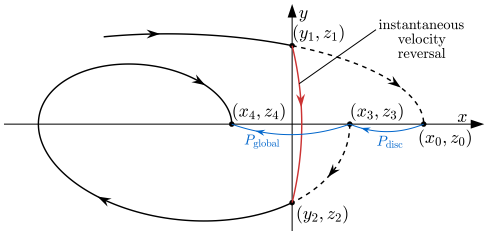

- However, Newton's method fails near grazing because $P_{\mathrm{disc},R}$ contains $\sqrt{x}$ (if $x < 0$, the method blows up!).

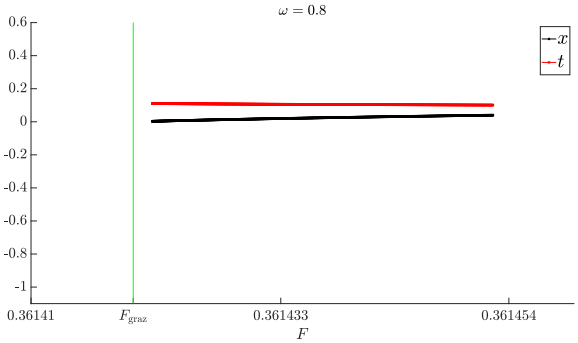

Numerics

- However, Newton's method fails near grazing because $P_{\mathrm{disc},R}$ contains $\sqrt{x}$ (if $x < 0$, the method blows up!).

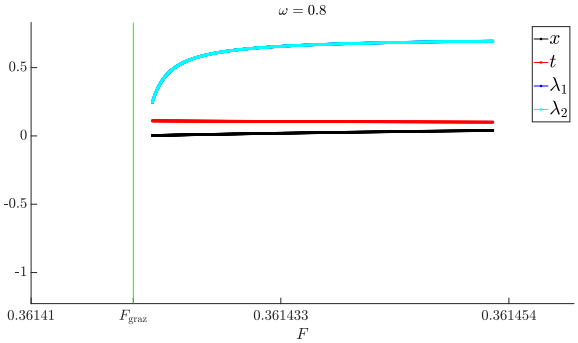

- So instead we guess (y_1, z_1), then compute (x_0, z_0), (y_2, z_2), and (x_3, z_3), and $(x_4, z_4) = P^p_{\text{global}}(x_3, z_3; F)$. Then let $V(y_1, z_1; F) = (x_4, z_4) - (x_0, z_0)$.

- So instead we guess (y_1, z_1), then compute (x_0, z_0), (y_2, z_2), and (x_3, z_3), and $(x_4, z_4) = P^p_{\text{global}}(x_3, z_3; F)$. Then let $V(y_1, z_1; F) = (x_4, z_4) - (x_0, z_0)$.
- The function V maps the impact velocity and z-value to the variation (or change) in displacement and z-value.

- So instead we guess (y_1, z_1), then compute (x_0, z_0), (y_2, z_2), and (x_3, z_3), and $(x_4, z_4) = P^p_{\text{global}}(x_3, z_3; F)$. Then let $V(y_1, z_1; F) = (x_4, z_4) - (x_0, z_0)$.
- The function V maps the impact velocity and z-value to the variation (or change) in displacement and z-value.
- We call the function V as the VIVID function that follows the zeros of a function mapping **V**elocity **I**nto **V**ariation **I**n **D**isplacement.

One-parameter bifurcation diagram

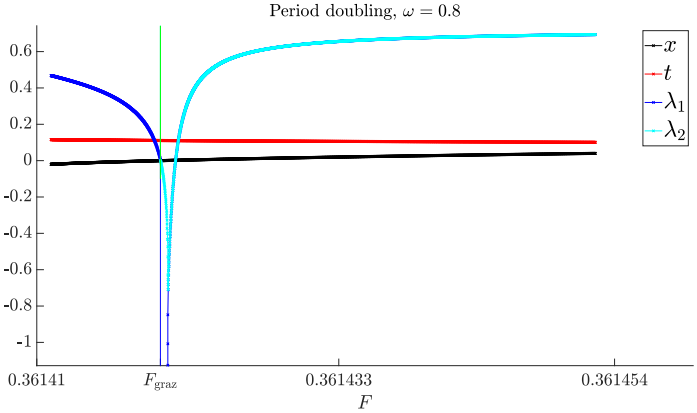

One-parameter bifurcation diagram

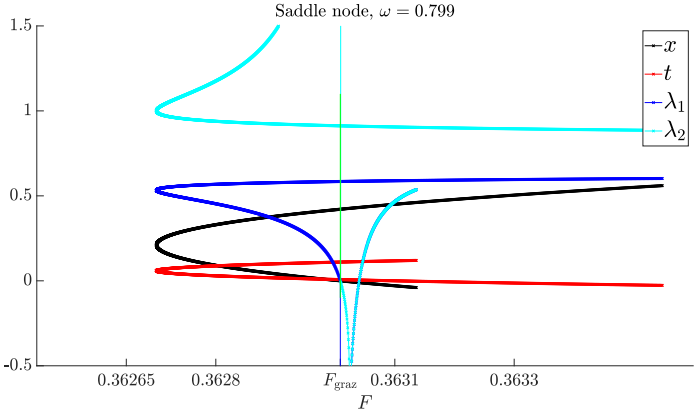

Two-parameter bifurcation diagram

- We are able to compute the two-parameter bifurcation diagram because of our new numerical tool.

Two-parameter bifurcation diagram

- We are able to compute the two-parameter bifurcation diagram because of our new numerical tool.
- The location of the codimension-two point is understood.

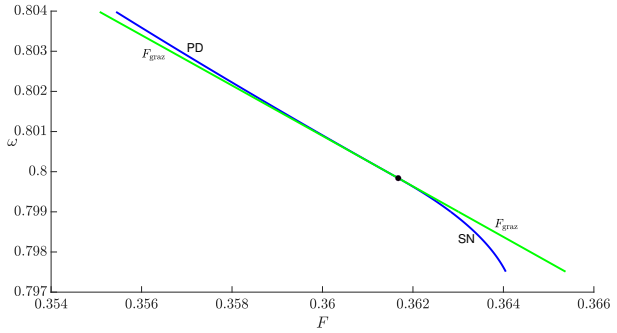

Resonance

- Branches of maximal periodic solutions emanate from the grazing bifurcation, either to the left or the right, and Nordmark (*Nonlinearity*, 2001) showed that this is determined by the values of τ and δ.

- Branches of maximal periodic solutions emanate from the grazing bifurcation, either to the left or the right, and Nordmark (*Nonlinearity*, 2001) showed that this is determined by the values of τ and δ.

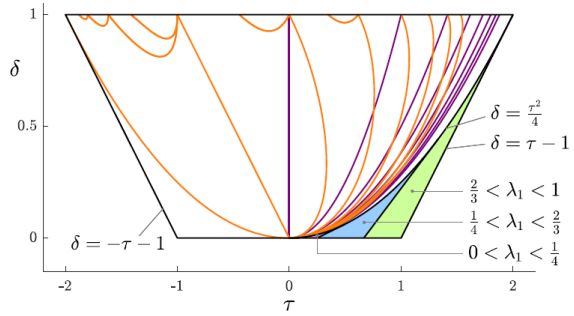

Figure: Division of the (τ, δ) plane.

- The eigenvalues of K are complex, and thus can be written as $\lambda_{1,2} = r\exp(\pm i\theta)$, where $r > 0$ and $0 < \theta < \pi$.

Resonance

- The eigenvalues of K are complex, and thus can be written as $\lambda_{1,2} = r\exp(\pm i\theta)$, where $r > 0$ and $0 < \theta < \pi$.
- Thus, we have $\tau = 2r\cos(\theta)$ and $\delta = r^2$.

Resonance

- The eigenvalues of K are complex, and thus can be written as $\lambda_{1,2} = r\exp(\pm i\theta)$, where $r > 0$ and $0 < \theta < \pi$.
- Thus, we have $\tau = 2r\cos(\theta)$ and $\delta = r^2$.
- The period-p solution changes from emanating to the left to emanating to the right when $\sin(p\theta) = 0$.

Resonance

- The eigenvalues of K are complex, and thus can be written as $\lambda_{1,2} = r\exp(\pm i\theta)$, where $r > 0$ and $0 < \theta < \pi$.
- Thus, we have $\tau = 2r\cos(\theta)$ and $\delta = r^2$.
- The period-p solution changes from emanating to the left to emanating to the right when $\sin(p\theta) = 0$.
- In particular, for $p = 1$, codimension-2 points occur when $\frac{\beta}{\omega} = \frac{n}{2}$, for some $n \in \mathbb{Z}$.

Resonance

- The eigenvalues of K are complex, and thus can be written as $\lambda_{1,2} = r\exp(\pm i\theta)$, where $r > 0$ and $0 < \theta < \pi$.
- Thus, we have $\tau = 2r\cos(\theta)$ and $\delta = r^2$.
- The period-p solution changes from emanating to the left to emanating to the right when $\sin(p\theta) = 0$.
- In particular, for $p = 1$, codimension-2 points occur when $\frac{\beta}{\omega} = \frac{n}{2}$, for some $n \in \mathbb{Z}$.
- For $p > 1$, codimenison-2 points occur when $\frac{\beta}{\omega} = n \pm \frac{1}{2p}$, for some $n \in \mathbb{Z}$

Discussion

- We have shown that the oscillator has a stable period-two solution near grazing because it is near resonance.

Discussion

- We have shown that the oscillator has a stable period-two solution near grazing because it is near resonance.
- We have developed a new numerical tool called **VIVID** using which the issue of "numerical algorithms falling off the side of square-root near grazing" is circumvented.

Discussion

- We have shown that the oscillator has a stable period-two solution near grazing because it is near resonance.
- We have developed a new numerical tool called **VIVID** using which the issue of "numerical algorithms falling off the side of square-root near grazing" is circumvented.
- We produce two-parameter bifurcation diagrams showing curves of saddle-node and period-doubling bifurcation emanating from a codimension-two grazing bifurcation.

Discussion

- We have shown that the oscillator has a stable period-two solution near grazing because it is near resonance.
- We have developed a new numerical tool called **VIVID** using which the issue of "numerical algorithms falling off the side of square-root near grazing" is circumvented.
- We produce two-parameter bifurcation diagrams showing curves of saddle-node and period-doubling bifurcation emanating from a codimension-two grazing bifurcation.
- However, it remains to unfold such codimension-two points theoretically (and we have started to work on this). Hopefully, this can explain why the SN curve bends away from F_{graz} faster than the PD curve.

Discussion

- We have shown that the oscillator has a stable period-two solution near grazing because it is near resonance.
- We have developed a new numerical tool called **VIVID** using which the issue of "numerical algorithms falling off the side of square-root near grazing" is circumvented.
- We produce two-parameter bifurcation diagrams showing curves of saddle-node and period-doubling bifurcation emanating from a codimension-two grazing bifurcation.
- However, it remains to unfold such codimension-two points theoretically (and we have started to work on this). Hopefully, this can explain why the SN curve bends away from F_{graz} faster than the PD curve.
- Would be intersting to see the behaviour when the damping ratio b limits to 0.

Neurons as Dynamical units

- Neurons represent the fundamental dynamical units of the nervous system
- The dynamics of neurons, like firing of action potentials, can be modeled as simple dynamical systems like ODEs or maps

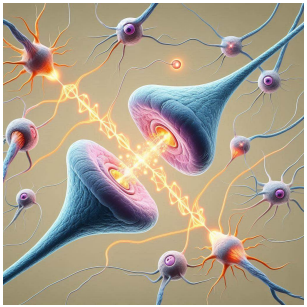

Figure: Two neurons connected by a synapse. (Powered by DALL-E 3)

Chialvo Map (Chialvo, 1995)

The two-dimensional neuron map is given by

$$x_{n+1} = x_n^2 e^{(y_n - x_n)} + k_0,$$
$$y_{n+1} = a y_n - b x_n + c.$$

- The state variables x and y represent the activation variable and recovery-like variable,
- a, b, c and k_0 are the system parameters,
- $a < 1$ is the time constant of recovery,
- $b < 1$ represents the activation dependence of the recovery process,
- c denotes the offset, and
- k_0 is the time-independent additive perturbation.

A Typical Phase Portrait

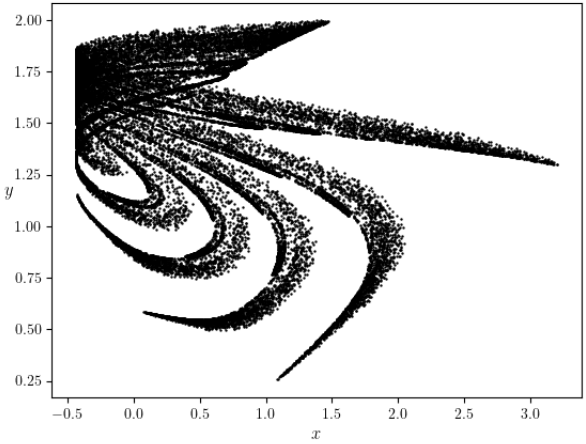

Electromagnetic flux

We describe the effects of electromagnetic flux on the system of neurons with **memristors**. The induction current due to electromagnetic flux is given by

$$\frac{dq(\phi)}{dt} = \frac{dq(\phi)}{d\phi}\frac{d\phi}{dt} = M(\phi)\frac{d\phi}{dt} = kM(\phi)x.$$

- ϕ: electromagnetic flux across the neuron membranes,
- k: electromagnetic flux coupling strength, &
- $M(\phi)$: memconductance of electromagnetic flux controlled memristor.

We consider the following memconductance function:

$$M(\phi) = \alpha + 3\beta\phi^2.$$

Improved Chialvo map under electromagnetic flux (Muni, Fatoyinbo, & Ghosh, 2022)

Under the action of electromagnetic flux, the system of Chialvo map is improved to the following map:

$$\begin{aligned} x_{n+1} &= x_n^2 e^{(y_n - x_n)} + k_0 + k x_n M(\phi_n), \\ y_{n+1} &= a y_n - b x_n + c, \\ \phi_{n+1} &= k_1 x_n - k_2 \phi_n, \end{aligned}$$

making the system a three-dimensional smooth map. The new variables α, β, k_1, k_2 represent the electromagnetic flux parameters.

Multistability

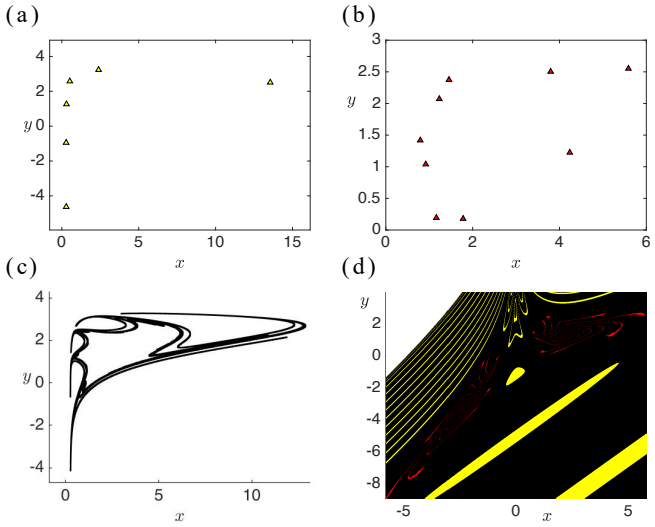

Bifurcation structures and antimonotonicity

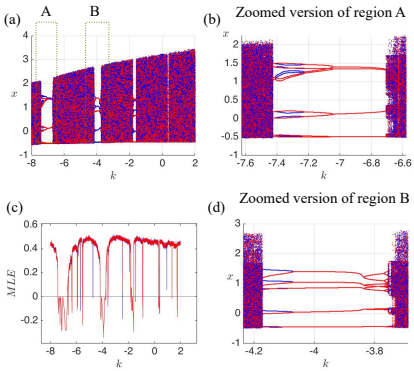

Figure: Bifurcation diagram of x with respect to k in panel (a). A maximal Lyapunov exponent diagram is shown in panel (b).

Bifurcation structures and antimonotonicity

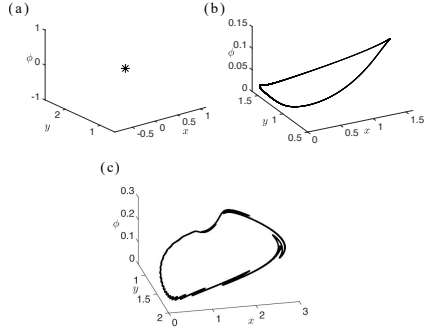

Figure: In (a) a stable fixed point is shown in the $x - y - \phi$ phase space for $a = 0.838$. After a supercritical Neimark-Sacker bifurcation, an attracting closed invariant curve is born as shown in (b) at $a = 0.841$. A chaotic attractor is then formed when a is increased to 0.88.

Table: Abbreviations of codimension-1 and codimension-2 bifurcations

Codimension-1			
Saddle-node (fold) bifurcation	LP	Neimerk-Sacker bifurcation	NS
Period-doubling (flip) bifurcation	PD		
Codimension-2			
Cusp	CP	Chenciner	CH
Generalized flip	GPD	Fold-Flip	LPPD
Flip-Neimark-Sacker	PDNS	Fold-Neimark-Sacker	LPNS
1:1 resonance	R1	1:2 resonance	R2
1:3 resonance	R3	1:4 resonance	R4

Numerical bifurcation analysis

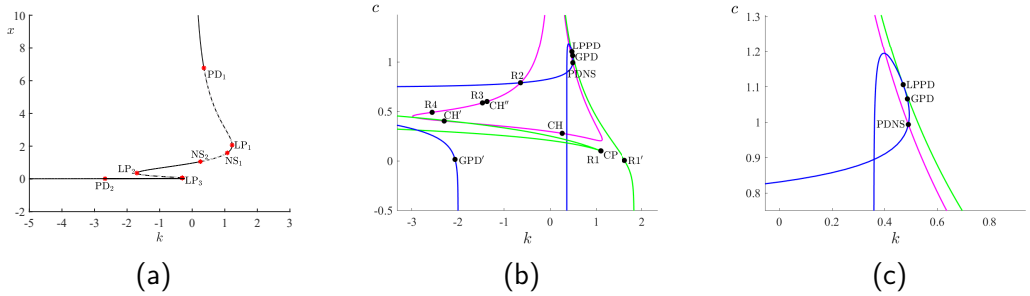

Figure: (a) Codimension-1 bifurcation diagram with k as bifurcation parameter. (b) Codimesion-2 bifurcation diagram in (k, c)-parameter plane. (c) Zoomed version of (b)

Bursting and spiking features

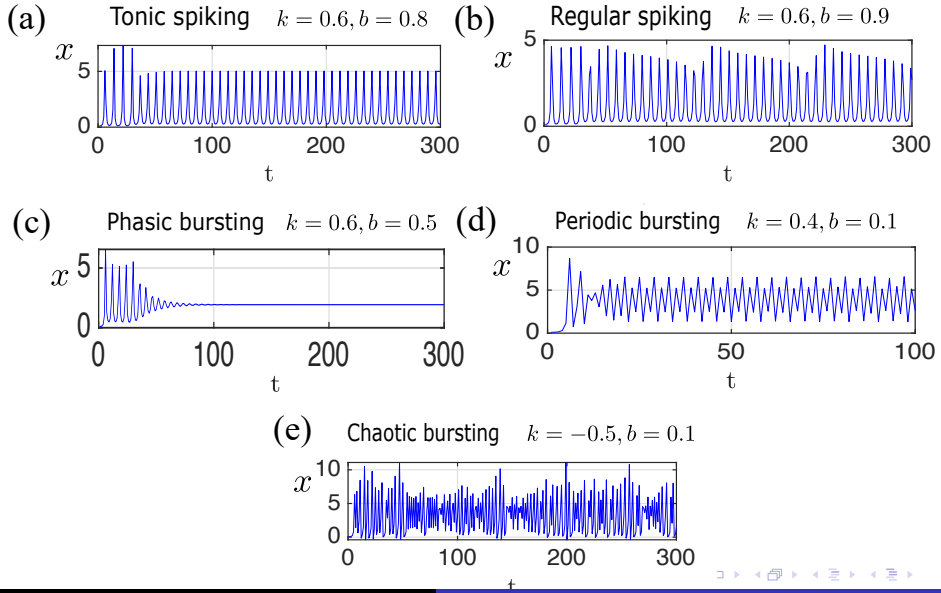

Discussion

- We have introduced a three-dimensional Chialvo neuron map under the effect of electromagentic flux.

Discussion

- We have introduced a three-dimensional Chialvo neuron map under the effect of electromagentic flux.
- We have performed numerical bifurcation analysis and portrayed different codimension-1 and codimension-2 bifurcation patterns.

Discussion

- We have introduced a three-dimensional Chialvo neuron map under the effect of electromagentic flux.
- We have performed numerical bifurcation analysis and portrayed different codimension-1 and codimension-2 bifurcation patterns.
- We aim to consider the model in a network and study the dynamical properties under noise.

Discussion

- We have introduced a three-dimensional Chialvo neuron map under the effect of electromagentic flux.
- We have performed numerical bifurcation analysis and portrayed different codimension-1 and codimension-2 bifurcation patterns.
- We aim to consider the model in a network and study the dynamical properties under noise.
- We also aim to study the influence of higher-order interaction (beyond piecewise interaction) on the synchronization manifold of the network.

Acknowledgements

The End

Thank you! Questions?